RESEARCH ARTICLE

**ADVANCED
PHOTONICS
RESEARCH**
Open Access

www.adpr-journal.com

High-Fidelity Information Transmission Through the Turbulent Atmosphere Utilizing Partially Coherent Cylindrical Vector Beams

Linxuan Yao, Hui Zhang, Yangsheng Yuan,* Yaru Gao, Chunhao Liang, Sergey A. Ponomarenko, and Yangjian Cai*

As the demand for high-capacity and high-fidelity communication systems continues to increase, addressing the challenges posed by noise and atmospheric turbulence disturbances is imperative. This study introduces and experimentally implements a novel free-space optical communication protocol. This protocol combines the advantages of reducing the spatial coherence of light at the source with the capabilities of convolutional neural networks at the receiver to encode and transmit optical images through a noisy link. Light beams that are robust against noise are generated and atmospheric turbulence is modeled in a laboratory setting by decreasing the degree of spatial coherence of the source. Eight orbital angular momentum states, four polarizations, and eight coherence states of a light source that generates partially coherent cylindrical vector beams are utilized. These elements are employed to achieve a 256-ary encoding/decoding data transmission within our protocol. This study is expected to catalyze further research into the utilization of partially coherent light and neural networks in the realm of free-space optical communications.

1. Introduction

Free-space optical (FSO) communications offer significant advantages, including wide bandwidth, high security, and high capacity.[1–4] Researchers have proposed various multiplexing methods, such as wavelength-division,[5,6] polarization-division,[7,8] mode-division,[9–11] and frequency-division multiplexing,[12,13] to enhance communication capacity. However, the increasing demand for wider bandwidths and the detrimental effects of atmospheric turbulence on transmitted signal quality necessitate the exploration of new degrees of freedom (DoFs) for light multiplexing within the FSO communication paradigm.

Meanwhile, orbital angular momentum (OAM) carrying light modes has garnered considerable attention in the realm of FSO communication.[1,14–16] Convolutional neural networks (CNNs) have emerged as valuable tools for correcting phase distortions caused by atmospheric turbulence[17–19] and for distinguishing different orthogonal OAM modes at the receiver plane.[20–25] The stable recognition of OAM modes facilitated by CNN is crucial for enhancing the accuracy of information transmission in high-capacity communications.[26–29] Furthermore, the utilization of fractional-order OAM carrying beams with minor topological charge increments of ≈0.01 between adjacent modes has enabled the encoding and transmission of optical information with exceptional resolution utilizing deep learning (DL) methods.[21] Sixteen encoding OAM modes were transmitted through a lengthy FSO communication link and successfully distinguished despite severe

L. Yao, H. Zhang, Y. Yuan, Y. Gao, C. Liang, Y. Cai
Shandong Provincial Engineering and Technical Center of Light Manipulations & Shandong Provincial Key Laboratory of Optics and Photonic Device
School of Physics and Electronics
Shandong Normal University
Jinan 250014, China
E-mail: yysheng@sdnu.edu.cn; yangjiancai@sdnu.edu.cn

L. Yao, H. Zhang, Y. Yuan, Y. Gao, C. Liang, Y. Cai
Collaborative Innovation Center of Light Manipulation and Applications
Shandong Normal University
Jinan 250358, China

L. Yao, H. Zhang, Y. Yuan, Y. Gao, C. Liang, Y. Cai
Joint Research Center of Light Manipulation Science and Photonic Integrated Chip of East China Normal University and Shandong Normal University
East China Normal University
Shanghai 200241, China

S. A. Ponomarenko
Department of Physics and Atmospheric Science
Dalhousie University
Halifax, NS B3H 4R2, Canada

S. A. Ponomarenko
Department of Electrical and Computer Engineering
Dalhousie University
Halifax, NS B3J 2X4, Canada

atmospheric turbulence, showcasing the effectiveness of artificial neural networks in this context.[30,31] The spatial intensity distribution of an OAM mode array can be leveraged to enhance the encoding capacity of FSO communications.[32,33]

In FSO communications, signal quality is affected seriously by the atmospheric turbulence.[34–37] Reducing the spatial coherence of a light source can mitigate the adverse effects of atmospheric turbulence.[38,39] Specifically, dark (antidark) diffraction-free beams, which feature dips (bumps) against an incoherent background,[40] can maintain their intensity profile in a turbulent atmosphere over a distance dependent on the turbulence strength. Moreover, such beams have considerably weaker scintillations compared with the statistically homogeneous Gaussian Schell-model (GSM) model.[41] In addition, the classical entanglement of partially coherent light associated with a twist phase,[42] unique to such light, can potentially increase the capacity of the FSO channel. Furthermore, low coherent light sources can reduce beam wander and scintillations,[43–45] whereas partially coherent vector beams offer advantages in mitigating turbulence effects.[46–48] These beams have been utilized for encryption, sensing, and imaging to alleviate turbulence-induced distortions.[49–52] In FSO communications, partially coherent beams have shown promise in reducing the bit error rate during signal transmission.[53–56] In this study, we propose combining the advantages of partially coherent light sources with the decoding power of CNNs to establish an FSO communication link that is robust to atmospheric turbulence. We successfully constructed a 256-ary encoding/decoding communication link with eight OAM states, four polarization states, and eight coherence lengths. To demonstrate the effectiveness of our protocol, we transmitted a high-fidelity 100×100 grayscale image of a cat through an FSO communication link subjected to atmospheric turbulence of variable strength.

2. Principle

2.1. Partially Coherent Cylindrical Vector Beams

The second-order statistical characteristics of partially coherent vector beams in any transverse plane where $z = \text{const} \geq 0$ can be described in terms of cross-spectral density terms expressed in a matrix form as follows[57]

$$W(r_1, r_2, z) = \begin{pmatrix} W_{xx}(r_1, r_2, z) & W_{xy}(r_1, r_2, z) \\ W_{yx}(r_1, r_2, z) & W_{yy}(r_1, r_2, z) \end{pmatrix} \quad (1)$$

where each matrix element represents a statistically homogeneous autocorrelation function of the form

$$W_{\alpha\beta}(r_1, r_2, z) = E_\alpha^*(r_1, \varphi_1, z) E_\beta(r_2, \varphi_2, z) \exp\left[-\frac{(r_1 - r_2)^2}{2\sigma^2}\right] \quad (2)$$

where $\alpha, \beta = x, y$; $\mathbf{r_i} = (r_i, \phi_i)$, $(i = 1, 2)$ represent the position vectors in the transverse plane of the beam, the asterisk denotes the complex conjugate, and σ represents the source coherence length assumed to be consistent across all matrix elements. Furthermore, the electric field $\mathbf{E}$ corresponds to a cylindrical vector beam source, expressed as follows[58]

$$\mathbf{E}(r_0, z = 0) = \frac{1}{2}R(r_0)\exp(il\varphi_0)\begin{pmatrix} 1 \\ -i \end{pmatrix} + \frac{1}{2}R(r_0)\exp(-il\varphi_0)\begin{pmatrix} 1 \\ i \end{pmatrix} \quad (3)$$

where

$$R(r_0) \propto \exp\left(-\frac{r_0^2}{w_0^2}\right)\left(\frac{2r_0^2}{w_0^2}\right)^{l/2} L_p^l\left(\frac{2r_0^2}{w_0^2}\right) \quad (4)$$

where $L_p^l(\bullet)$ denotes a Laguerre polynomial of order l and radial index p and w_0 represents the beam width at the source.

The intensity of a partially coherent cylindrical vector beam transmitted by a linear polarizer with the polarization axis at an angle φ with the x-axis can be expressed as follows

$$I = W_{xx}(\mathbf{r}, \mathbf{r}, z)\cos^2\varphi + W_{yy}(\mathbf{r}, \mathbf{r}, z)\sin^2\varphi + W_{xy}(\mathbf{r}, \mathbf{r}, z)\sin 2\varphi \quad (5)$$

The intensity distributions of partially coherent cylindrical vector beams corresponding to different coherence states, topological charges of the source, and polarizer axis directions are shown in **Figure 1**. Parameters, such as $w_0 = 0.8$ mm, $\lambda = 632.8$ nm, $C_n^2 = 5 \times 10^{-15}$ m$^{-2/3}$, $z = 80$ cm, $p = 0$, and $l = 1, 2$, and 3, were chosen for illustration. As shown in Figure 1, the source coherence length significantly impacts the intensity distribution, with the beam petals appearing blurry in the low coherence limit.
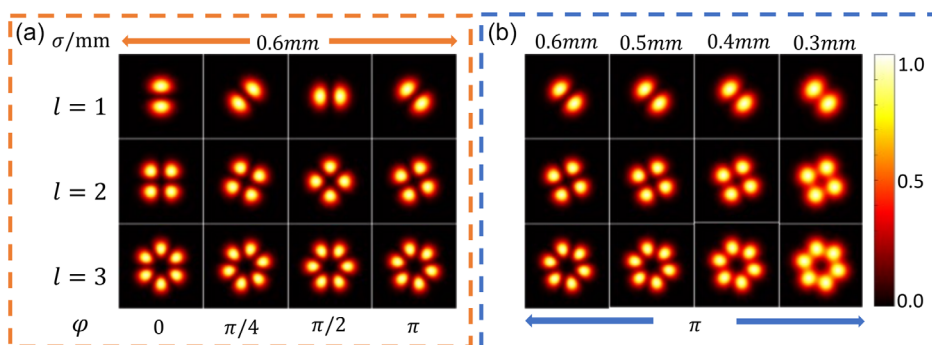

Figure 1. Intensity of the partially coherent cylindrical vector beams through a linear polarizer. a) Coherent length $\sigma = 0.6$ mm for different OAM modes $l = 1, 2$, and 3 and polarization directions $\varphi = 0, \pi/4, \pi/2, 3\pi/4$ in orange box. b) polarization direction $\varphi = \pi$ for different OAM modes $l = 1, 2$, and 3 and coherent lengths $\sigma = 0.6, 0.5, 0.4, 0.3$ mm in a blue box.

The subsequent section demonstrates the application of CNN to recognize these subtle differences.

2.2. CNN Model

The utilization of CNNs enables the differentiation of intensity distribution shapes of partially coherent cylindrical vector beams across variable coherence and polarization states, as well as different topological charges. A CNN was established in MATLAB, following the AlexNet architecture[59] (**Figure 2**). Our CNN comprises five blocks for feature extraction and three fully connected (FC) layers (dense layers) for classification. The input data for the CNN are a 100×100-pixel grayscale images. The feature extraction process involves convolutional layers, nonlinear activation functions, and max-pooling layers. The convolutional layers extract local conjunctions of features from the preceding layer,[20] whereas the nonlinear activation functions enable the network to learn complex data and make accurate predictions.[60] A rectified linear unit (ReLU) function ($f(x) = \max(0, x)$) is utilized as a nonlinear activation function with a high-computing speed.[61] To reduce computational complexity and prevent overfitting, a maximum pooling layer is utilized. Following the feature extraction process, three FC layers generate output data, with the ReLU function being replaced by a SoftMax function in the final FC layer. The SoftMax function is ideal for multiclassification tasks and provides the probability of each output from an FC layer.

Detailed parameters are shown, and an output size for each layer of the CNN is listed in **Table 1**. A dropout layer, randomly set at 50% for each training epoch, was positioned at the end of an FC layer to prevent overfitting.[62] The weights and biases of the convolutional and max pooling layers were selected from the pretrained Alexnet architecture.[60] The variable X represents the number of categories, which can be changed adjusted based on the dataset.

This study utilized partially coherent cylindrical vector beams with the same OAM mode ($l = 2$), four polarization directions ($\varphi = 0, \pi/4, \pi/2, 3\pi/4$), and eight coherent lengths ($\sigma = 0.65, 0.6, 0.55, 0.5, 0.45, 0.4, 0.35,$ and 0.3 mm). As shown in **Figure 3**, the dataset comprises 32 categories, that is, $X = 32$. The dataset was generated using Equation (5), with parameters matching those in Figure 1. Each of the 32 categories contained 1600 images, with 50 images per category. The training and validation datasets were split in a 7:3 ratio, with an initial learning rate of 0.001. The training results, indicated in **Figure 4**, indicate

Table 1. Specifications of the CNN model, with X representing the number of output categories.

	Layer	Setting			Output
		Num. and size	Padding	Stride	
–	Conv2D1, ReLU1	64, (6×6)	0	2	$48 \times 48 \times 64$
B1	Maxpool1	(2×2)	0	2	$24 \times 24 \times 64$
	Conv2D2, ReLU2	64, (4×4)	2	1	$25 \times 25 \times 64$
B2	Maxpool2	(2×2)	0	2	$12 \times 12 \times 64$
B3	Conv2D3, ReLU3	128, (3×3)	1	1	$12 \times 12 \times 128$
B4	Conv2D4, ReLU4	128, (3×3)	1	1	$12 \times 12 \times 128$
B5	Conv2D5, ReLU5	256, (3×3)	1	1	$12 \times 12 \times 256$
	Maxpool5	(2×2)	0	2	$6 \times 6 \times 256$
FC6	Dense6, ReLU6	–			$1 \times 1 \times 1024$
	Dropout6	0.5			
FC7	Dense7, ReLU7	–			$1 \times 1 \times 1024$
	Dropout7	0.5			
FC8	Dense8, ReLU8	–			$1 \times 1 \times X$
	Dropout8	–			

that the network achieved near-perfect training and validation accuracy, approaching 100%. This demonstrates the effectiveness of the CNN network in classifying partially coherent cylindrical vector beams. The coherence length, topological charge, and polarization direction, serving as three DoFs, can be utilized as multiplexed communication DoFs to enhance the channel capacity.

3. Experimental Section

3.1. Experimental Generation of Partially Coherent Cylindrical Vector Beams

To generate a partially coherent cylindrical vector beam from the GSM source, a rotating ground-glass disk (RGGD) was utilized, as shown in **Figure 5**. A laser beam with a wavelength of 632.8 nm and horizontally polarized light was first expanded using a beam expander and then focused by a lens L_1 (focal length $f_1 = 150$ mm). This process, through the RGGD, resulted in a nearly incoherent beam with Gaussian statistics. This incoherent beam was then collimated using a lens L_2 (focal length
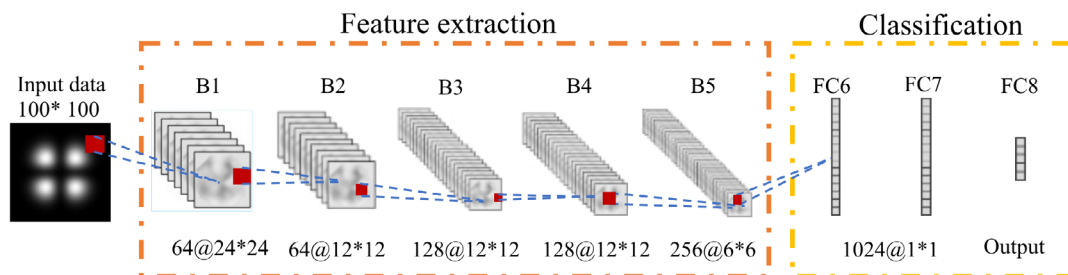

Figure 2. Structure of the CNN model including input data, feature extraction, and classification. Bi (i = 1, 2, 3, 4, and 5), block; FC, fully connected layers. The annotation of num.@num.*num. represents the number of channels@length * width of the corresponding feature map.
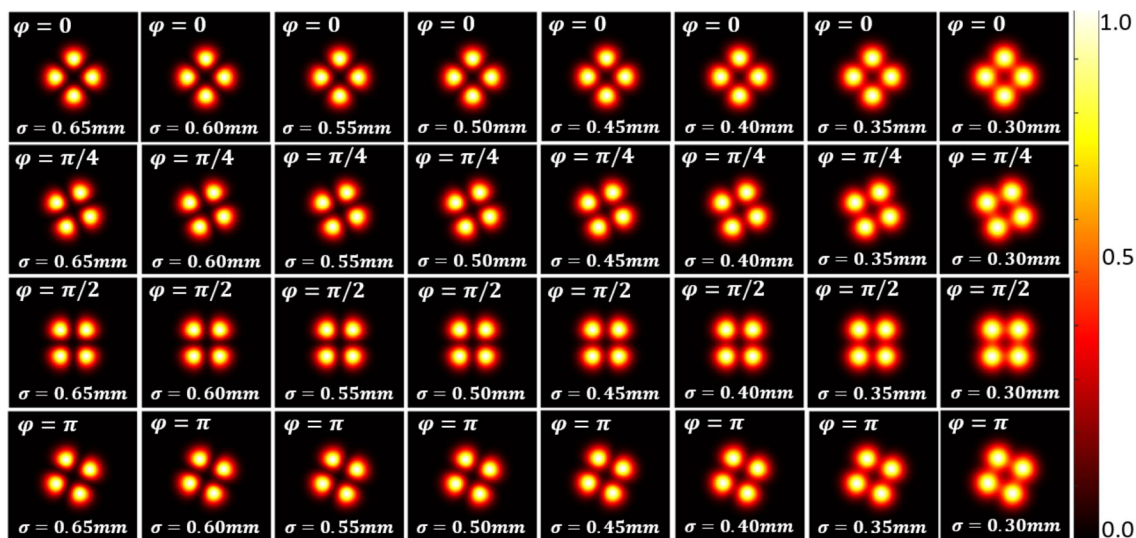
Figure 3. Simulated dataset. The horizontal and vertical coordinates represent the coherence length and polarization direction of a single OAM mode, respectively.

$f_2 = 200$ mm) with the RGGD positioned in the focal plane of L_2. The resulting beam was transmitted through a Gaussian amplitude filter (GAF) to obtain a GSM beam. The spot size and coherence length of the beam can be controlled by adjusting the position of L_1 relative to the RGGD. The method for measuring the coherence length of the source beam is examined in the Supporting Information. For precise control of the coherence length, L_1 was placed on a computer-controlled electric-moving stage.

The GSM beam was then directed onto a spatial light modulator (SLM1) loaded with spiral-phase holograms corresponding to $l = 1, 2, 3, 4, 5, 6, 7,$ and 8. The diffracted beam traversed a 4f imaging system (focal length $f_3 = f_4 = 100$ mm) and was

filtered by a circular aperture in the back focal plane of a lens L_3. This process results in a partially coherent Laguerre–Gaussian (LG) beam with the desired topological charge l in the first diffraction order of the SLM1. Before reaching SLM2, the partially coherent LG beam must be polarized along an axis making at a 45° angle with the x-axis. SLM2, which only responded to horizontal polarization, was loaded with a phase hologram corresponding to a topological charge $-2l$. Consequently, the resulting beam carried a topological charge of $-l$ $(-2l + l = -l)$ in its x-polarized component and that of l in the y-polarized component. A quarter-wave plate was utilized to convert the x- and y-polarizations into left- and right-handed circular polarizations, generating a partially coherent cylindrical
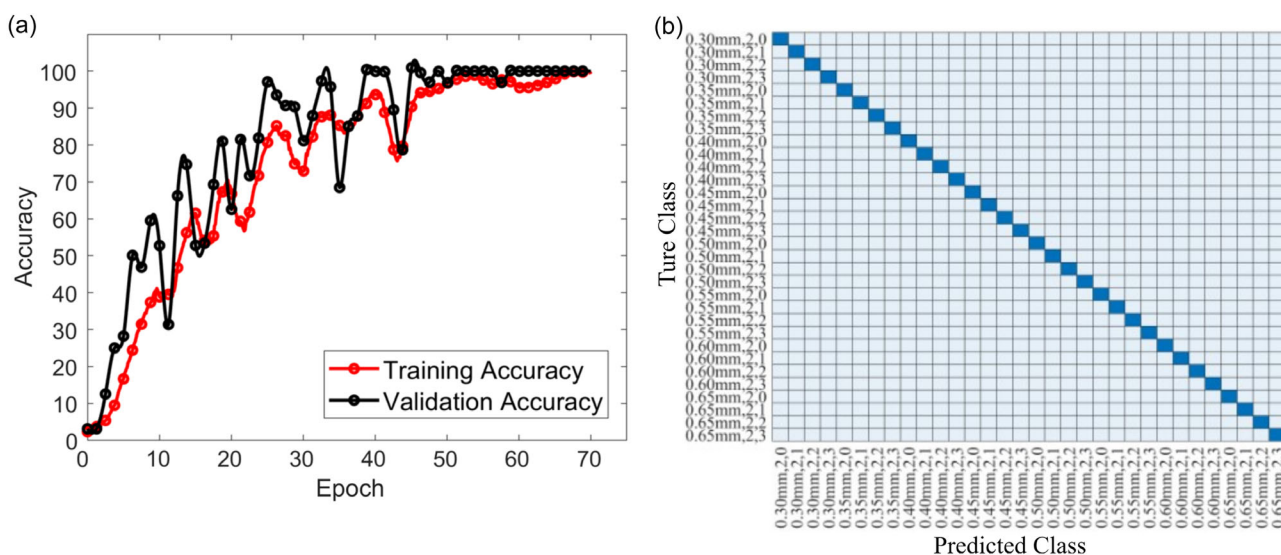

Figure 4. CNN training results. a) Red and black lines indicate the training and validation accuracy, respectively. b) Corresponding confusion matrix. Coordinate labels represent the coherent length and polarization angle ($\varphi = 0, \pi/4, \pi/2, 3\pi/4$ is replaced with 0, 1, 2, and 3), respectively.
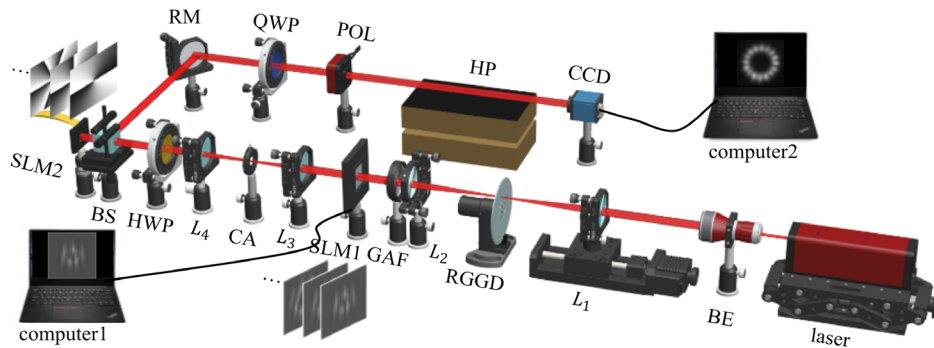
2400137 (4 of 9)

Figure 5. Experimental setup for testing our FSO communication protocol in the laboratory. BE, beam expander; L_1, L_2, L_3, and L_4, lenses; RGGD, rotating ground-glass disk; GAF, Gaussian amplitude filter; SLM1, SLM2, spatial light modulator; CA, circular aperture; HWP, half-wave plate; QWP, quarter-wave plate; BS, beam splitter; RM, reflecting mirror; POL, polarizer; HP, hotplate; CCD, charge-coupled device.
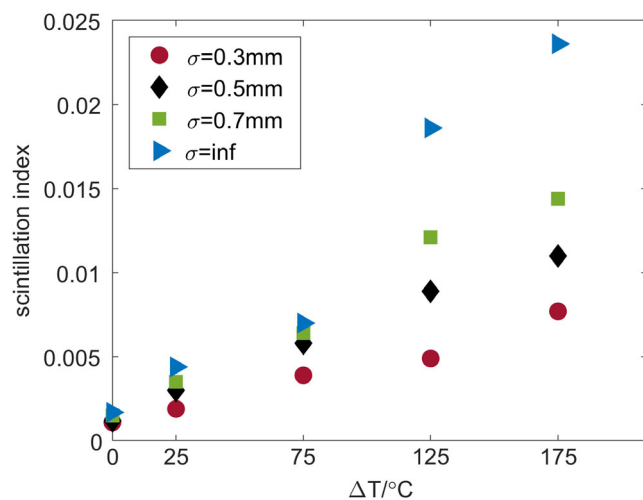

Figure 6. Measured scintillation index of Gaussian beams with different coherence lengths as a function of the difference compared with that at room temperature.

A total of 3000 frames were captured, each representing the intensity distribution of an ensemble member within a turbulent medium. This results in a dataset that can be expressed in matrix form $I_n(\overline{x}_n, \overline{y}_n)$, where $I_n(\overline{x}_n, \overline{y}_n)$ denotes the intensity at the centroid of each image captured by a CCD, x and y denote transverse spatial coordinates, and $1 \leq n \leq 3000$.

The measured scintillation index is presented as a function of the temperature difference in **Figure 6**. The results indicated an increase in scintillation with increasing plate temperature. Simultaneously, the scintillations decreased as the source coherence diminished, aligning with the existing literature.[45,47,48]

3.2. Encoding and Decoding Communication Link

Our FSO communication protocol utilized a 256-ary encoding system, incorporating DoFs related to the source coherence length, topological charge, and polarization state. Eight beam configurations were selected with topological charges ($l = 1, 2, 3, 4, 5, 6, 7,$ and 8), which are generated by SLM1 and SLM2 controlled by computers 1 and 2, respectively. Additionally, lens L_1, mounted on an electric moving stage and controlled by computer 1, adjusted the source coherence length accordingly. Further technical details of our measurement technique can be found in the Supporting Information. A polarizer was positioned on a motorized rotation stage (controlled by computer 1) to accurately generate four polarization states of the beam corresponding to four polarizer angles ($\varphi = 0, \pi/4, \pi/2, \pi$). Signal beams transmitted through a simulated turbulence stretch created by a hotplate with a CCD were captured for analysis.

A CNN was adopted to differentiate intensity distributions of partially coherent cylindrical vector beams based on their coherence lengths, topological charges, and polarization states. To train and test the CNN, 256 beam intensity patterns were utilized, each corresponding to 250 images captured at different hot plate temperatures within the set 25, 50, 100, 150, 200, measured in degrees Celsius, with room temperature set at 25 °C. The 250 intensity distribution images of each type were divided into training and validation datasets, with an image resolution of 100 × 100 pixels. Each subset contained 175 images for training
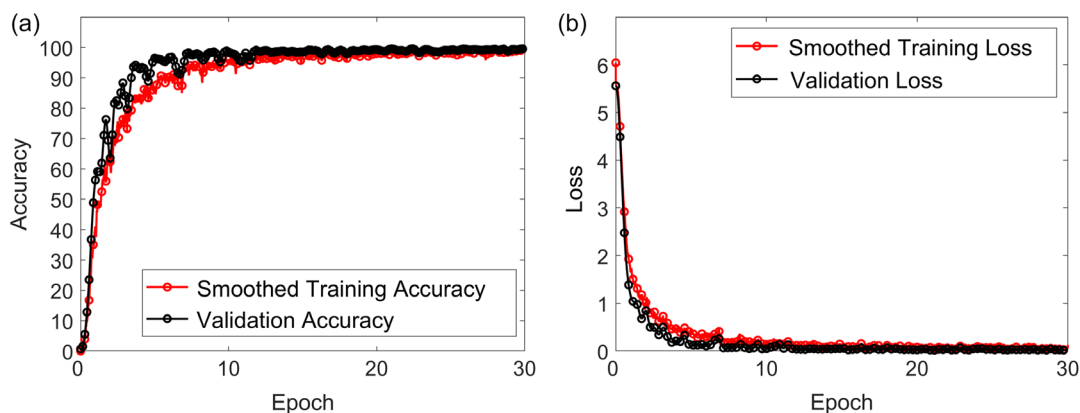
vector beam with a spatial structure corresponding to an LG function.

Furthermore, a hotplate with dimensions of $42 \times 30 \times 23$ cm (length × width × height) was positioned in the path of the generated beam to simulate atmospheric turbulence effects. The turbulence strength was controlled by adjusting the temperature difference between the hot plate and the room. The intensity distribution data for different polarization states of the source can be obtained using polarizers and a charge-coupled device (CCD). The turbulence induced by the hot plate disrupted the phase of any incident cylindrical vector beam, leading to intensity fluctuations. These fluctuations were quantified by the scintillation index, a normalized intensity autocorrelation function[63] calculated over an ensemble of N realizations corresponding to the number of frames captured by the camera. The scintillation index of a Gaussian beam with a variable coherence state at the source that propagated through a given layer of simulated turbulence was measured to determine the strength of the turbulence in the laboratory (refer to the Supporting Information).

Figure 7. Training results of the designed CNN: a) accuracy and b) loss.

and 75 for validation, resulting in a 7:3 ratio. The output size of the last FC layer of the network was adjusted to $X = 256$ to train the dataset. The training results are shown in **Figure 7**, indicating that the smoothed training accuracy approached the validation accuracy as the number of epochs increased. We could not obtain data from our CNN model that does not exhibit overfitting. The validation and training sets differed during training. The validation dataset was utilized to assess the accuracy of the CNN at each epoch, allowing us to effectively distinguish between images of beam intensity distributions within our protocol. The trained CNN was validated using the validation dataset, with the accuracy of the neural network determined as the proportion of correctly classified samples. Our training results showed a minimum validation loss level of 6.6×10^{-4}, whereas the validation accuracy reached an impressive 99.34%.

The results of image transmission using our protocol over a noisy link are shown in **Figure 8**. A 100×100 pixel grayscale image of a cat with grayscale values ranging from 0 to 255 was utilized to demonstrate our protocol. Each grayscale value corresponds to a specific source beam characterized by coherence length, topological charge, and polarization state. The grayscale values from the cat image were read off and encoded with the corresponding beam types, as outlined in a

detailed encoding chart provided in the Supporting Information. A computer controlled the electric moving stage and loaded the hologram onto SLM1 and SLM2 to generate the corresponding beam structure required for encoding the image. Each image captured by the CCD was recognized by our trained CNN. These recognized image types were subsequently restored to the corresponding grayscale values by the computer, resulting in a matrix of grayscale values that enabled the reconstruction of the cat image.

The received images of the cat, reconstructed using a grayscale values matrix for different turbulence strengths of the communication link (different hotplate temperatures), are shown in **Figure 9**. Incorrectly received pixels were marked in red. A remarkable accuracy rate of 100% can be achieved for a turbulence-free communication link and $\approx 96.57\%$ for the noisy link corresponding to a hotplate temperature of $T = 200\,°C$, simulating severe atmospheric turbulence. Overall, our experimental results validate that FSO image transmission can be effectively performed through a noisy channel with turbulence levels ranging from weak to strong. Furthermore, we demonstrate that utilizing source coherence can effectively enhance the potential of FSO communication in noisy environments.
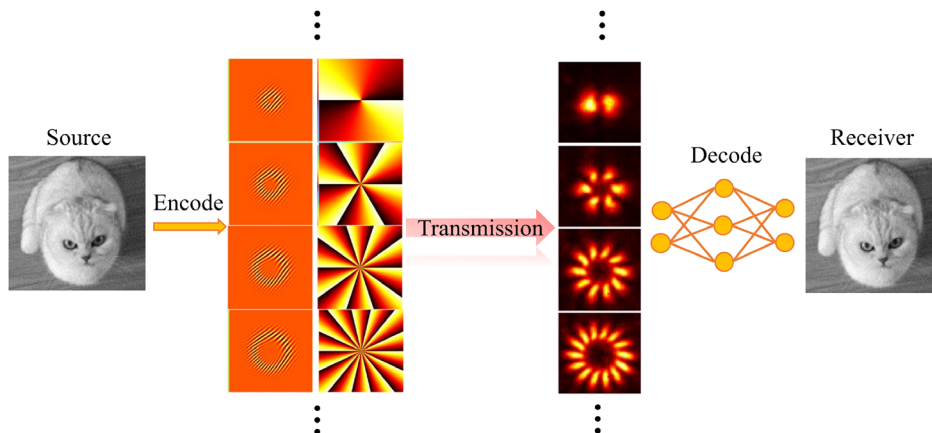

Figure 8. Cat image transmission utilizing the 256-bit multiplexing system.

**ADVANCED
SCIENCE NEWS**

www.advancedsciencenews.com

**ADVANCED
PHOTONICS
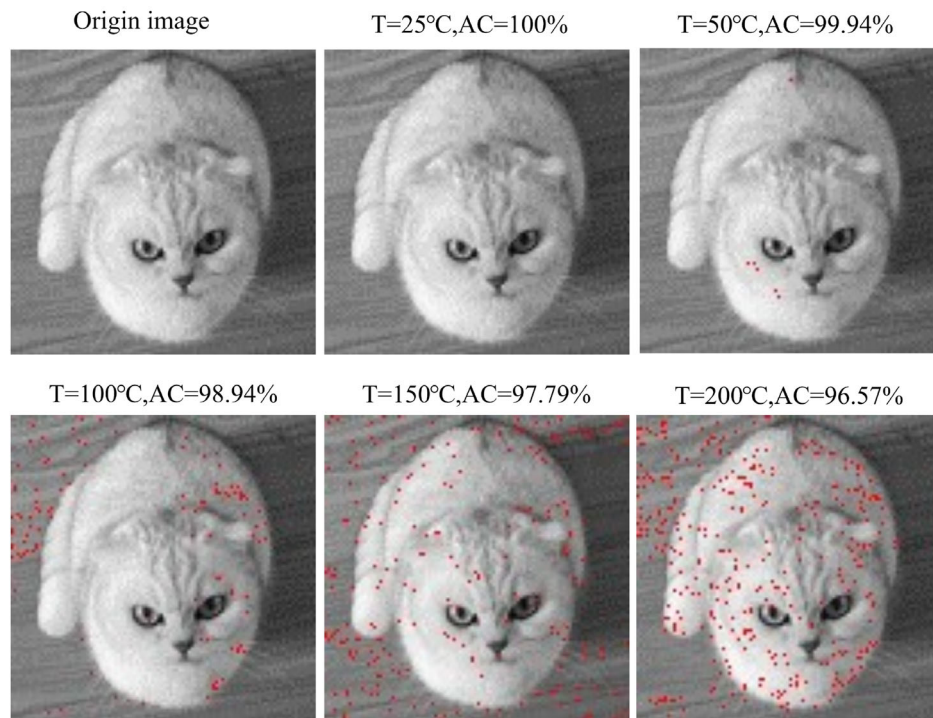RESEARCH**
Open Access

www.adpr-journal.com

Figure 9. Transmitted image data. Cat images with grayscale values ranging from 0 to 255 encoded in our communication system through a free-space channel with different turbulence strengths. The red pixels indicate the incorrectly received data. AC, accuracy; T, hotplate temperature.

4. Conclusion

This study introduced a novel FSO communication protocol that leveraged the reduced coherence of the light source and the advanced decoding capabilities of neural networks, specifically CNN, to ensure the high quality of transmitted information. By adjusting the spatial coherence of the sources, the beams generated by such a source could withstand the corrosive effects of atmospheric turbulence, whereas the DL capabilities of the CNN ensured that the received images closely resemble the transmitted images within our protocol. In our proof-of-principle experiment, we utilized a hot plate with controllable temperature to simulate the impact of atmospheric turbulence. A 256-ary encoding/decoding system incorporated eight adjustable coherence lengths, eight OAM modes, and four polarization states to successfully transmit a gray image of a cat. Through the application of the CNN, we could accurately recover the transmitted image with 100% accuracy in ideal conditions and with 96.7% accuracy in a noisy communication link that mimicked a strong fluctuation regime of a turbulent atmosphere. These experimental findings provide valuable insights for future research on integrating DL techniques into FSO communications utilizing structured random light.

Supporting Information

Supporting Information is available from the Wiley Online Library or from the author.

Conflict of Interest

The authors declare no conflict of interest.

Author Contributions

Linxuan Yao: Data curation: (equal); Software: (equal); Writing—original draft: (equal). **Hui Zhang**: Writing—original draft: (equal). **Yangsheng Yuan**: Funding acquisition: (equal); Supervision: (equal); Writing—review & editing: (equal). **Yaru Gao**: Data curation: (equal). **Chunhao Liang**: Software: (equal). **Sergey A**. **Ponomarenko**: Writing—review & editing: (equal). **Yangjian Cai**: Funding acquisition: (lead); Project administration: (lead); Supervision: (lead).

Data Availability Statement

The data that support the findings of this study are available from the corresponding author upon reasonable request.

Keywords

cylindrical vector beams, high-fidelity, partially coherent, turbulent atmosphere

[1] J. Wang, J.-Y. Yang, I. M. Fazal, N. Ahmed, Y. Yan, H. Huang, Y. Ren, Y. Yue, S. Dolinar, M. Tur, A. E Willner, *Nat. Photonics* **2012**, *6*, 488.

[2] J. Du, J. Wang, *Opt. Lett.* **2015**, *40*, 4827.

[3] J. Wang, J. Liu, S. Li, Y. Zhao, J. Du, L. Zhu, *Nanophotonics* **2022**, *11*, 645.

[4] X. Wang, Y. Song, F. Pang, Y. Li, Q. Zhang, L. Zhuang, X. Guo, Y. Ju, S. Yang, X. He, Y. Yang, *Opt. Lasers Eng.* **2021**, *137*, 106352.

[5] S. Wengerowsky, S. K. Joshi, F. Steinlechner, H. Hübel, R. Ursin, *Nature* **2018**, *564*, 225.

[6] K. Zou, K. Pang, H. Song, J. Fan, Z. Zhao, H. Song, R. Zhang, H. Zhou, A. Minoofar, C. Liu, X. Su, N. Hu, A. McClung, M. Torfeh, A. Arbabi, M. Tur, A. E. Willner, *Nat. Commun.* **2022**, *13*, 7662.

[7] L. Deng, J. Deng, Z. Guan, J. Tao, Y. Chen, Y. Yang, D. Zhang, J. Tang, Z. Li, Z. Li, S. Yu, G. Zheng, H. Xu, C. Qiu, S. Zhang, *Light: Sci. Appl.* **2020**, *9*, 101.

[8] K. Singh, I. Nape, W. T. Buono, A. Dudley, A. Forbes, *Laser Photonics Rev.* **2023**, *17*, 2200844.

[9] H. Zhang, X. Xiao, Y. Gao, J. Li, B. J. Hoenders, Y. Cai, Y. Yuan, *Appl. Phys. Lett.* **2023**, *123*, 21.

[10] S. Kruk, F. Ferreira, N. Mac Suibhne, C. Tsekrekos, I. Kravchenko, A. Ellis, D. Neshev, S. Turitsyn, Y. Kivshar, *Laser Photonics Rev.* **2018**, *12*, 1800031.

[11] H. Feng, X. Chen, R. Zhu, Y. Xiong, Y. Chen, Y. Lu, F. Xu, *Opto-Electron. Adv.* **2024**, *7*, 230202–1.

[12] Y. Cai, S. Shi, Y. Zhou, Y. Li, J. Yu, W. Li, L. Li, *Phys. Rev. Appl.* **2023**, *19*, 044079.

[13] S. Zhang, D. Tsonev, S. Videv, S. Ghosh, G. A. Turnbull, I. D. Samuel, H. Haas, *Optica* **2015**, *2*, 607.

[14] Z. Zhu, M. Janasik, A. Fyffe, D. Hay, Y. Zhou, B. Kantor, T. Winder, R. W. Boyd, G. Leuchs, Z. Shi, *Nat. Commun.* **2021**, *12*, 1666.

[15] H. Song, R. Zhang, N. Hu, H. Zhou, X. Su, H. Song, K. Zou, K. Pang, C. Liu, D. Park, et al., *Nanophotonics* **2022**, *11*, 885.

[16] R. Zhang, N. Hu, H. Zhou, K. Zou, X. Su, Y. Zhou, H. Song, K. Pang, H. Song, A. Minoofar, Z. Zhao, C. Liu, K. Manukyan, A. Almaiman, B. Lynn, R. W. Boyd, M. Tur, A. E. Willner, *Nat. Photonics* **2021**, *15*, 743.

[17] S. Lohani, R. T. Glasser, *Opt. Lett.* **2018**, *43*, 2611.

[18] J. Hao, X. Lin, Y. Lin, H. Song, R. Chen, M. Chen, K. Wang, X. Tan, *Opt. Lett.* **2021**, *46*, 4168.

[19] K. Wang, L. Song, C. Wang, Z. Ren, G. Zhao, J. Dou, J. Di, G. Barbastathis, R. Zhou, J. Zhao, E. Y. Lam, *Light: Sci. Appl.* **2024**, *13*, 4.

[20] Y. LeCun, Y. Bengio, G. Hinton, *Nature* **2015**, *521*, 436.

[21] Z. Liu, S. Yan, H. Liu, X. Chen, *Phys. Rev. Lett.* **2019**, *123*, 183902.

[22] Z. Mao, H. Yu, M. Xia, S. Pan, D. Wu, Y. Yin, Y. Xia, J. Yin, *Phys. Rev. Appl.* **2020**, *13*, 034063.

[23] H. Zhou, Y. Wang, X. Li, Z. Xu, X. Li, L. Huang, *Appl. Phys. Lett.* **2021**, *119*, 4.

[24] X. Wang, H. Wei, M. Jin, B. Xu, J. Chen, *Opt. Express* **2022**, *30*, 11165.

[25] J. Guo, Y. Zhang, H. Ye, L. Wang, P. Chen, D. Mao, C. Xie, Z. Chen, X. Wu, M. Xiao, Y. Zhang, *ACS Photonics* **2023**, *10*, 757.

[26] Y. Shi, Z. Ma, H. Chen, Y. Ke, Y. Chen, X. Zhou, *Front. Phys.* **2024**, *19*, 32205.

[27] J. Zhu, M. Fan, Y. Pu, H. Li, S. Wang, *Opt. Lett.* **2023**, *48*, 2692.

[28] W. Chen, Q. Lin, W. Chen, Z. Zhang, Z. Zhuang, Z. Su, L. Zhang, *Opt. Lett.* **2023**, *48*, 1886.

[29] H. Tan, J. Deng, R. Zhao, X. Wu, G. Li, L. Huang, J. Liu, X. Cai, *Laser Photonics Rev.* **2019**, *13*, 1800278.

[30] M. Krenn, R. Fickler, M. Fink, M. Handsteiner, M. Malik, T. Scheidl, R. Ursin, A. Zeilinger, *New J. Phys.* **2014**, *16*, 113028.

[31] M. Krenn, J. Handsteiner, M. Fink, R. Fickler, R. Ursin, M. Malik, A. Zeilinger, *Proc. Natl. Acad. Sci.* **2016**, *113*, 13648.

[32] Z. Wan, Y. Shen, Z. Wang, Z. Shi, Q. Liu, X. Fu, *Light: Sci. Appl.* **2022**, *11*, 144.

[33] G. Jing, L. Chen, P. Wang, W. Xiong, Z. Huang, J. Liu, Y. Chen, Y. Li, D. Fan, S. Chen, *Results Phys.* **2021**, *28*, 104619.

[34] J. Broky, G. A. Siviloglou, A. Dogariu, D. N. Christodoulides, *Opt. Express* **2008**, *16*, 12880.

[35] L. Andrews, R. Phillips, in *Laser Beam Propagation Through Random Media*, Press Monographs, SPIE Optical Engineering Press, Bellingham, Washington **1998**.

[36] S. Popoff, G. Lerosey, M. Fink, A. C. Boccara, S. Gigan, *Nat. Commun.* **2010**, *1*, 81.

[37] Y. Ren, H. Huang, G. Xie, N. Ahmed, Y. Yan, B. I. Erkmen, N. Chandrasekaran, M. P. Lavery, N. K. Steinhoff, M. Tur, S. Dolinar, M. Neifeld, M. J. Padgett, R. W. Boyd, J. H. Shapiro, A. E. Willner, *Opt. Lett.* **2013**, *38*, 4062.

[38] G. Gbur, *JOSA A* **2014**, *31*, 2038.

[39] M. W. Hyde, *APL Photonics* **2024**, *9*, 10.

[40] M. Yessenov, B. Bhaduri, H. E. Kondakci, M. Meem, R. Menon, A. F. Abouraddy, *Optica* **2019**, *6*, 598.

[41] Z. Xu, X. Liu, Y. Cai, S. A. Ponomarenko, C. Liang, *JOSA A* **2022**, *39*, C51.

[42] S. A. Ponomarenko, *Opt. Lett.* **2021**, *46*, 5958.

[43] L. Liu, W. Liu, F. Wang, X. Peng, D.-Y. Choi, H. Cheng, Y. Cai, S. Chen, *Light: Sci. Appl.* **2024**, *13*, 131.

[44] Y. Huang, A. Zeng, Z. Gao, B. Zhang, *Opt. Lett.* **2015**, *40*, 1619.

[45] A. Nair, Q. Li, S. N. Stechmann, *Opt. Lett.* **2023**, *48*, 3865.

[46] Z. Zhang, G. Li, Y. Liu, H. Wang, B. J. Hoenders, C. Liang, Y. Cai, J. Zeng, *Opto-Electron. Sci.* **2024**, *3*, 240001.

[47] S. Joshi, S. N. Khan, P. Senthilkumaran, B. Kanseri, *Phys. Rev. A* **2021**, *103*, 053502.

[48] Z. Dong, Y. Chen, F. Wang, Y. Cai, A. T. Friberg, T. Setälä, *Phys. Rev. Appl.* **2022**, *18*, 034036.

[49] Y. Liu, Y. Chen, F. Wang, Y. Cai, C. Liang, O. Korotkova, *Opto-Electron. Adv.* **2021**, *4*, 210027.

[50] B. Redding, M. A. Choma, H. Cao, *Nat. Photonics* **2012**, *6*, 355.

[51] X. Lu, Z. Wang, Q. Zhan, Y. Cai, C. Zhao, *Adv. Photonics* **2024**, *6*, 046002.

[52] G. Massaro, B. Barile, G. Scarcelli, F. V. Pepe, G. P. Nicchia, M. D'Angelo, *Laser Photonics Rev.* **2024**, 2301155.

[53] J. C. Ricklin, F. M. Davidson, *JOSA A* **2003**, *20*, 856.

[54] Y. Kato, K. Mima, N. Miyanaga, S. Arinaga, Y. Kitagawa, M. Nakatsuka, Yamanaka, C., *Phys. Rev. Lett.* **1984**, *53*, 1057.

[55] G. Gbur, T. Visser, in *Progress in Optics*, Vol. 55, Elsevier, Amsterdam **2010**, pp. 285–341.

[56] X. Li, Y. Wang, X. Liu, Y. Ma, Y. Cai, S. A. Ponomarenko, X. Liu, *Appl. Phys. Lett.* **2024**, *124*, 214103.

[57] E. Wolf, *Phys. Lett. A* **2003**, *312*, 263.

[58] M. Cao, Z. Xie, Y. Zhong, T. Lei, W. Zhang, S. Liu, X. Yuan, *Nanophotonics* **2023**, *12*, 1753.

[59] A. Krizhevsky, I. Sutskever, G. E. Hinton, *Adv. Neural Inf. Process. Syst.* **2012**, *1*, 1097.

[60] V. E. Balas, S. S. Roy, D. Sharma, P. Samui, in *Handbook of Deep Learning Applications*, Vol. *136*, Springer, New York **2019**.

[61] A. L. Maas, A. Y. Hannun, A. Y. Ng, in *Proc. ICML*, Vol. *30*, Atlanta, GA, June **2013**, p. 3.

[62] N. Srivastava, G. Hinton, A. Krizhevsky, I. Sutskever, R. Salakhutdinov, *J. Mach. Learn. Res.* **2014**, *15*, 1929.

[63] X. Liu, Y. Shen, L. Liu, F. Wang, Y. Cai, *Opt. Lett.* **2013**, *38*, 5323.